

Salt-dependent rheology and surface tension of protein condensates using optical traps

Louise M. Jawerth,^{1,2} Mahdiye Ijavi,¹ Martine Ruer,¹ Shambaditya Saha,¹ Marcus Jahnel,^{1,3} Anthony A. Hyman,¹ Frank Jülicher,^{2,*} and Elisabeth Fischer-Friedrich^{1,2,3,†}

¹Max-Planck-Institut für Zellbiologie und Genetik,
Pfotenhauerstraße 108, 01307 Dresden, Germany

²Max-Planck-Institut für Physik komplexer Systeme, Nöthnitzerstraße 38, 01187 Dresden, Germany

³Biotechnology Center, Technische Universität Dresden, Tatzberg 47-49, 01307 Dresden, Germany

(Dated: December 7, 2018)

An increasing number of proteins with intrinsically disordered domains have been shown to phase separate in buffer to form liquid-like phases. These protein condensates serve as simple models for the investigation of the more complex membrane-less organelles in cells. To understand the function of such proteins in cells, the material properties of the condensates they form are important. However, these material properties are not well understood. Here, we develop a novel method based on optical traps to study the frequency-dependent rheology and the surface tension of PGL-3 condensates as a function of salt concentration. We find that PGL-3 droplets are predominantly viscous but also exhibit elastic properties. As the salt concentration is reduced, their elastic modulus, viscosity and surface tension increase. Our findings show that salt concentration has a strong influence on the rheology and dynamics of protein condensates suggesting an important role of electrostatic interactions for their material properties.

Introduction. A fundamental question of biology is to understand the spatial organization of cells into compartments of distinct chemical composition and activity. Many cellular compartments are bounded by membranes. However, cells also possess compartments that are not bounded by membranes. Examples are germline granules, cajal bodies, nucleoli and stress granules. It has been shown in recent years that many membrane-less compartments are protein condensates forming soft materials that coexist with the cytoplasm or nucleoplasm and often exhibit liquid-like properties [1–10].

Liquid-like compartments typically contain one or two scaffold proteins which are required for compartment formation and to which RNA and other proteins co-localize [1, 4, 11]. Many scaffold proteins phase separate *in vitro* when introduced into physiological buffer resulting in the condensation of liquid-like droplets. A well-studied example of a phase-separating scaffold protein is PGL-3 - a major component of P-granules, the germline granules of the nematode worm *Caenorhabditis elegans* [2, 6, 11, 12]. This and other protein droplets serve as models for the soft materials that form the more complex liquid-like compartments in cells [5–7, 10, 12, 13]. The material properties of protein droplets are important to understand the biological function of protein condensates in cells - for example when they serve as biochemical reaction centers, which requires rapid diffusion of components, or when they serve as structural elements, which may require some degree of elasticity. However, the material properties and rheology have not yet been fully characterized. Active microrheological methods that could provide such information for micron-sized droplets are currently lacking.

The saturation concentration of protein phase separation *in vitro* depends on buffer conditions such as salt concen-

tration, pH or the presence of RNA [6, 7, 10, 12–14]. The salt and pH dependence of the saturation concentration suggests a role of charge and electrostatic interactions in protein phase separation.

In this letter, we develop a novel active microrheology method to determine the frequency-dependent rheology of micron-sized PGL-3 droplets as a function of salt concentration using optical traps. Protein droplets are deformed via two opposing adhered beads trapped by optical traps (Fig. 1a,b). Surface tension γ and the complex shear modulus $G^*(\omega) = G'(\omega) + iG''(\omega)$ that characterize the droplet material properties can be obtained using a theoretical analysis of force balances associated with droplet deformation in the optical trap setup. Here G' and G'' denote the storage and loss moduli, respectively.

Force balance of droplet deformation. The microrheology setup based on a dual optical trap is shown in Fig. 1a,b. The droplet is deformed by moving one trap. The resulting force balance involves forces F_1 and F_2 exerted on the droplet by the traps with stiffnesses k_1 and k_2 , as well as viscous drag exerted on the droplet by the fluid with friction coefficient ξ (Fig. 1c). In the overdamped regime, force balance requires

$$F_1 + F_2 = \xi v \quad , \quad (1)$$

where v is the droplet velocity. The difference of F_1 and F_2 is balanced by forces exerted by the deformed droplet. For time periodic forces $F_{1,2} = \tilde{F}_{1,2} \exp(i\omega t) + c.c.$ and droplet diameter $x_d = x_{d,0} + \tilde{x}_d \exp(i\omega t) + c.c.$ with angular frequency ω , we have

$$(\tilde{F}_1 - \tilde{F}_2)/2 = \chi^*(\omega) \tilde{x}_d \quad . \quad (2)$$

Here, the tilde denotes the complex amplitude of the Fourier mode at angular frequency ω and *c.c.* refers to the complex conjugate. In Eq. (2), $\chi^*(\omega) = \chi'(\omega) + i\chi''(\omega)$

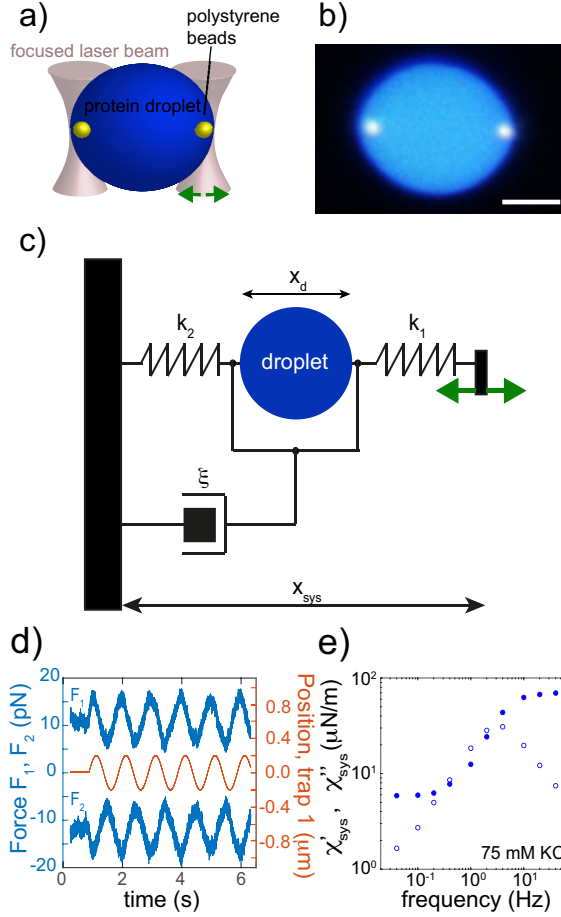


FIG. 1. Microrheology setup based on a dual optical trap. a) Schematic. b) Fluorescent micrograph of protein droplet during the measurement. Scale bar: $5 \mu\text{m}$. c) Mechanical circuit equivalent of measurement setup. d) Exemplary experimental output during oscillatory droplet deformation: position of optical trap 1 (red) and forces associated to optical traps 1 and 2 (blue) at frequency 1 Hz and 75 mM KCl. e) Exemplary system spring constants χ_{sys}^* (●), χ_{sys}'' (○) from the measurement of a protein droplet with a diameter of $12.2 \mu\text{m}$ at a salt concentration of 75 mM KCl.

characterizes the complex frequency-dependent spring constant of the droplet response, where $\chi'(\omega)$ and $\chi''(\omega)$ denote the real and imaginary part of the complex spring constant, respectively. For an oscillatory trap movement $\tilde{v} = i\omega(\tilde{x}_d/2 + \tilde{F}_2/k_2)$. The complex spring constant of the entire system (droplet in series with two optical traps) is

$$\chi_{sys}^*(\omega) = (\tilde{F}_1 - \tilde{F}_2)/(2\tilde{x}_{sys}) \quad (3)$$

where x_{sys} is the distance between the trap centers (Fig. 1c). The distance x_{sys} can differ from the droplet diameter x_d because the beads can move out of the trap centers. The complex spring constant of the droplet can be related to the complex spring constant of the system

using

$$x_{sys} = (F_1/k_1 - F_2/k_2) + x_d \quad (4)$$

We find

$$\chi^* = \frac{\chi_{sys}^*(4k_1k_2 + i\xi\omega(k_1 + k_2))}{2k_1(2k_2 + i\xi\omega) - 4\chi_{sys}^*(k_1 + k_2 + i\xi\omega)} \quad (5)$$

Droplet mechanics in the optical trap. To determine the protein droplet's surface tension γ as well as the complex frequency dependent shear modulus $G^*(\omega)$ in the optical trap setup, we need to relate these material properties to the complex spring constant χ^* defined in Eq. (2). The mechanical droplet stress satisfies the force balance

$$\partial_i \sigma_{ij} = 0 \quad (6)$$

For small deformations in the low Reynold's number regime, the constitutive material equation of an incompressible droplet material can be written as

$$\tilde{\sigma}_{ij} = -\tilde{p} \cdot \delta_{ij} + G^*(\omega) [\partial_i \tilde{u}_j + \partial_j \tilde{u}_i] \quad (7)$$

where p denotes pressure and u_i is the displacement vector with components $i, j = x, y, z$. Stress boundary conditions on the surface of a spherical droplet of radius R read in spherical coordinates r, θ, ϕ

$$-p_{ext} - \sigma_{rr}(R, \theta) = 2\gamma H \quad (8)$$

$$\sigma_{r,\theta}(R, \theta) = 0 \quad (9)$$

Here, p_{ext} is the local normal force per area exerted on the droplet surface and H denotes the mean curvature of the weakly deformed droplet surface. Forces mediated by adherent beads of radius r_{bead} are captured by a time periodic pressure distribution with complex amplitude $\tilde{p}_{ext} = P_0(\Theta(\theta - \pi + \theta_0) + \Theta(\theta_0 - \theta))$ on the droplet surface (Fig. 2a), where Θ denotes the Heaviside function and $\theta_0 = r_{bead}/R$.

Using Eqn. (6-9), we calculate the time-dependent deformation field $u_r(r, \theta, t)$ of droplet material using a stream function approach and an expansion in spherical harmonics, see Supplement. The time dependent droplet diameter can be expressed as $x_d(t) = 2(R + u_r(R, 0, t))$ and the difference of optical trap forces is given by $F_1(t) - F_2(t) = \oint dA p_{ext}$. We then obtain the complex spring constant of the droplet response χ^* as a function of G^* and γ using Eq. (2), see Supplement. This droplet spring constant is related to the spring constant of the entire optical trap system through Eq. (5).

Droplet spring constant in simple cases. We first discuss the droplet and system spring constants for a droplet consisting of a Newtonian fluid. In this case, the complex shear modulus $G^* = i\omega\eta$ where η is the viscosity. Using the approach described above, we determine the droplet spring constant χ^* and the system spring constant χ_{sys}^* .

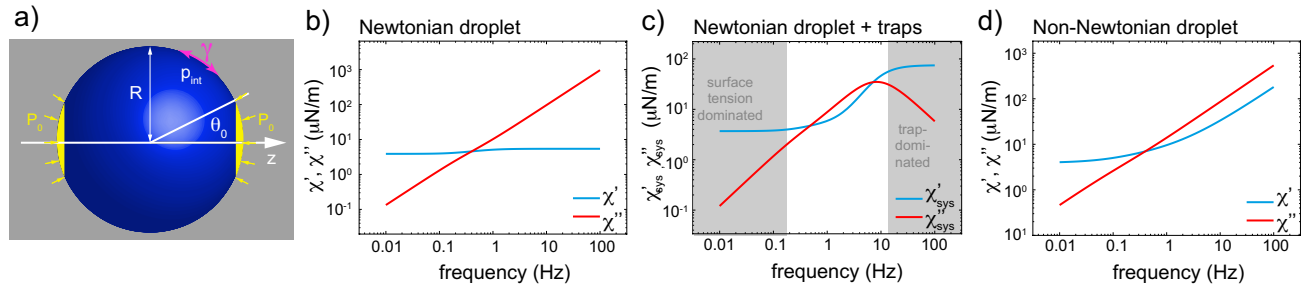


FIG. 2. Spring constants for a Newtonian and non-Newtonian-droplet subject to polar forcing. a) Droplets are subject to an oscillatory pressure P_0 applied in a dome-shaped region at the poles. b) Complex spring constant χ^* of a Newtonian droplet with surface tension. c) Complex system spring constant of a Newtonian droplet in series with two identical traps. For low frequencies, the spring constant is dominated by surface tension (grey zone, l.h.s.). For high frequencies, the two traps dominate the spring constant and χ'_{sys} approaches $k/2$ (grey zone, r.h.s.). Outside of this trap-dominated regime, the loss modulus is governed by the viscous properties of the droplet material. d) Spring constant of a non-Newtonian droplet formed by a power law fluid, i.e. $G^*(\omega) = A\pi\omega^\beta(\csc(\pi\beta/2) + i\sec(\pi\beta/2))/2$, and with surface tension. Parameters are $\theta_0 = 0.1$, $R = 5 \mu\text{m}$, $\gamma = 3 \mu\text{N/m}$, $\eta = 0.5 \text{ Pa s}$, $A = 0.2 \text{ Pa}$, $\beta = 0.8$, $k_1 = k_2 = 150 \text{ pN}/\mu\text{m}$ and $\xi = 6\pi\eta_b R$, where $\eta_b = 10^{-3} \text{ Pa s}$.

The droplet spring constant as a function of frequency is shown in Fig. 2b. The real part of the spring constant (blue) stems from surface tension. The imaginary part (red) is associated with viscosity.

The system spring constant for a Newtonian droplet is shown in Fig. 2c. At low frequencies, the response of the system is dominated by the droplet surface tension, corresponding to a plateau in the real part (see gray low-frequency region Fig. 2c). The intermediate frequency range is dominated by droplet viscosity. At high frequencies, the system response is dominated by the optical traps (see gray high-frequency region Fig. 2c).

We also consider a droplet composed of a non-Newtonian fluid with a power law rheology in both loss and storage moduli $G' \sim G'' \sim \omega^\beta$ with exponent β . The corresponding droplet spring constant reveals droplet surface tension at low frequencies and power-law rheology at high frequencies, Fig. 2d.

Salt dependent material properties of PGL-3 droplets. We performed measurements on PGL-3 protein droplets formed in buffer (25mM HEPES, 1mM DTT, pH 7.5) at four different salt concentrations (75 mM, 115 mM, 150 mM and 180 mM KCl). Polystyrene beads of $1 \mu\text{m}$ diameter added to the buffer were brought into adhesive contact with protein droplets (see Supplement). Radii of droplets used were between $5\text{-}9 \mu\text{m}$. Droplets were deformed at frequencies between 0.04 and 40 Hz. Forces exerted by both optical traps and the position of the mobile trap center were recorded. From this data, we first determined the system spring constant $\chi_{sys}^*(\omega)$ using Eq. (3) (Fig. 1e). The frequency dependent spring constant exhibits the three regimes discussed above (compare Fig. 1e and Fig. 2c): a low frequency regime dominated by surface tension, an intermediate regime and a high frequency regime dominated by the traps (Fig. 1e).

We then determined the complex spring constant of uni-

axial droplet elongation χ^* using Eq. (5) (Fig. 3a). From this data, we first determined the surface tension γ in the low frequency regime using

$$\gamma \approx \chi'(\omega)/(1.25 + 4.36\theta_0^2) \quad , \quad (10)$$

valid for small $\theta_0 = r_{bead}/R \ll 1$ (see Supplement). We then obtain the complex shear modulus G^* by accounting for surface tension effects from the droplet spring constant (Fig. 3b and Supplement). For modulus $R|G^*(\omega)| \gg \gamma$ and small θ_0 we use

$$G^*(\omega) \approx \frac{(\chi^*(\omega) - (1.75 + 6.31\theta_0^2)\gamma)}{R(0.58 + 3.42\theta_0^2)} \quad (11)$$

(see Supplement). Fig. 3c-f show storage and loss moduli as a function of frequency averaged over several experiments for four different salt concentrations. Loss moduli G'' increased approximately linearly for increasing frequency (Fig. 3b-f). Corresponding viscosity values range from $\eta = 0.1$ to 1 Pa s . Storage moduli at a reference frequency of 10 Hz ranged between values of 0.1 and 15 Pa. Both, viscosities and storage moduli decreased with increasing salt concentration (Fig. 3g and i). The associated loss tangent G''/G' exhibited a sharp drop when salt concentration was reduced to 75 mM, suggesting a more solid-like rheology at lower salt concentrations (Fig. 3j). The estimated surface tension γ was about $5 \mu\text{N/m}$ for 75 mM salt and decreased steadily for increasing salt concentrations with $\gamma \approx 1 \mu\text{N/m}$ at 180 mM salt (Fig. 3h and Supplement).

To test our new method, we measured viscosity and surface tension using two established methods. Using passive bead-tracking microrheology, we estimated a viscosity $\eta = 0.7 \pm 0.1 \text{ Pa s}$ at 75 mM salt which is in excellent agreement with our active microrheology results (Fig. 3g and Supplement). Furthermore, we analysed

thermal fluctuations of droplet shape to measure surface tension $\gamma \approx 1.4 \mu\text{N/m}$ at 180 mM salt, consistent with our new method.

The surface tension and viscosity of polyelectrolyte condensates have been studied theoretically [17, 18]. In Fig. 3h, we compare the predicted salt-dependence of surface tension to our data and find good agreement. Furthermore, the salt dependence of a characteristic time is also in agreement with this theory (see supplemental Fig. S6).

Discussion. Here, we used a novel technique with optical traps to characterize the rheology of PGL-3 protein droplets. We find that newly formed PGL-3 droplets consist of a viscoelastic material with liquid-like material properties that depend on salt concentration. Viscosities range from 0.1 to 1 Pa s for decreasing salt concentrations from 180 to 75 mM. The storage modulus is smaller than the loss modulus, but approaches the loss modulus from below for frequencies larger than 10 Hz. Furthermore, we obtain more precise values of surface tension than previous methods. Values depend on salt concentration and range from $1 \mu\text{N/m}$ to $5 \mu\text{N/m}$ for decreasing salt concentrations from 180 to 75 mM. Such low values of surface tension are consistent with values estimated for colloidal systems with weak interactions but much smaller than typical air-water or oil-water systems [15, 16]. Notably, our viscosity and surface tension estimates for PGL-3 droplets *in vitro* are consistent with estimates for P-granules *in vivo* suggesting that *in vitro* PGL-3 is a good model system for the physics and material properties of P-granules *in vivo* [2]. Interestingly, our viscosity and surface tension values for PGL-3 are between one to two orders of magnitude smaller than estimates for droplets of the P-granule protein LAF-1 formed *in vitro* [12].

Viscosities of PGL-3 droplets exhibit a strong salt dependence qualitatively similar to salt-dependent viscosity estimates reported for phase-separated LAF-1 by passive bead-tracking micro-rheology (Fig. 3g) [12]. The decrease in storage moduli, loss moduli and surface tensions for increasing salt concentrations suggests that screened electrostatic interactions play an important role in protein condensates and their material properties. As salt concentration is increased, interactions become weaker because of screening effects. Interestingly, synthetic polyelectrolytes show a similar dependence of rheology and surface tension on salt concentration as the protein condensates studied here [17, 18].

In conclusion, our measurements show that protein condensates are complex polymeric liquids with viscoelastic material properties that can be regulated by salt concentration. We obtain our results using a novel optical trap based rheometer suitable for micron-sized probes. This method does not rely on thermodynamic equilibrium. We expect that our work will trigger more studies that lead to a deep understanding of the physics of protein droplets

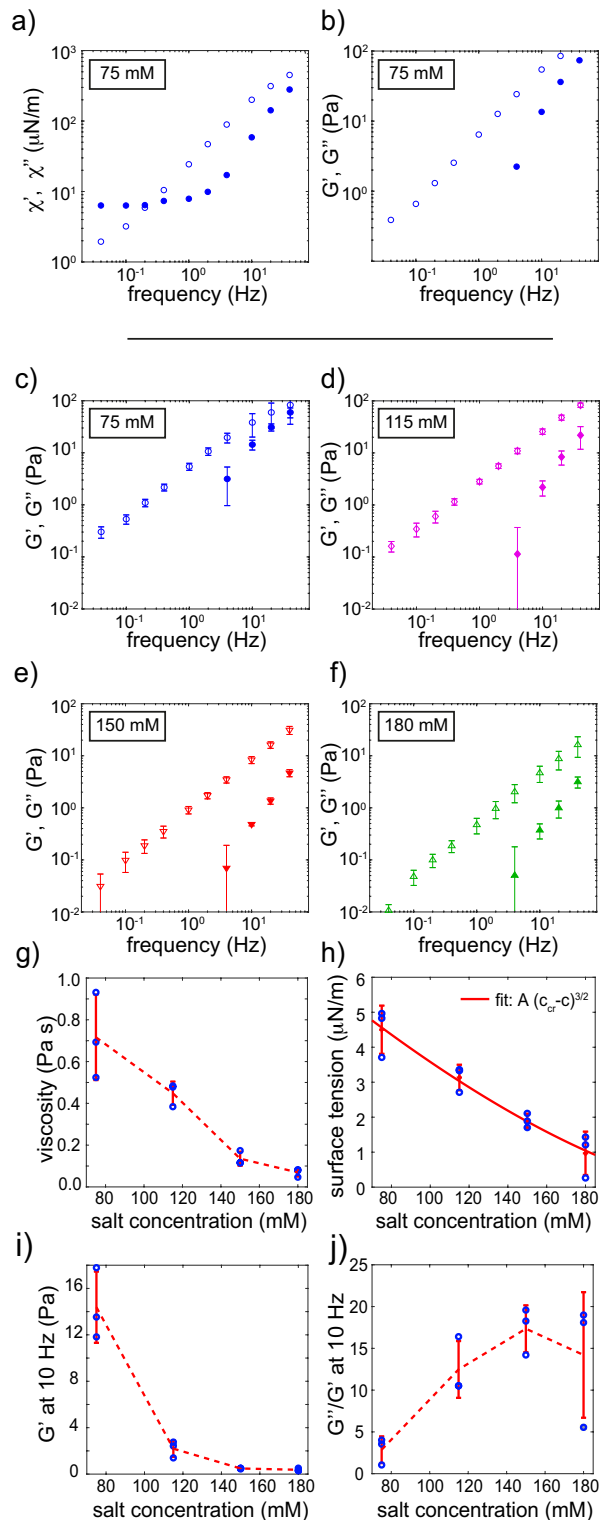


FIG. 3. Salt dependent material properties of PGL-3 droplets. a-b) Spring constants χ' (\bullet), χ'' (\circ) and reconstructed moduli G' (\bullet), G'' (\circ) for one droplet. (Corresponding χ_{sys}^* shown in Fig. 1e) c-f) Ensemble average of G' (closed symbols), G'' (open symbols) of the droplet material at salt concentrations of 75, 115, 150 and 180 mM KCl. Error bars indicate standard deviations ($n=3$). g-j) Salt dependence of viscosity found using a linear fit to the loss modulus ($G'' = \omega\eta$ where η is the viscosity) (g), surface tension (h), storage modulus at 10 Hz (i) and loss tangent at 10 Hz (j). In panel h, we show a fit of the theoretically predicted decay of surface tension in dependence of salt concentration c (solid red line) [18], where $c_{cr} = 243$ mM is the fitted critical salt concentration.

and their phase behavior in biological cells.

ACKNOWLEDGMENTS

We would like to thank Marcus Jahnel and Stephan Grill for useful discussions and the staff of LUMICKS for their technical assistance. Furthermore, we would like to thank the following Services and Facilities of the MPI-CBG for their support: The Protein Expression Purification and Characterization (PEPC) facility.

* Corresponding author: julicher@pks.mpg.de

† Corresponding author: elisabeth.fischer-friedrich@tudresden.de

- [1] A. A. Hyman, C. A. Weber, and F. Jülicher, *Annual Review of Cell and Developmental Biology* **30**, 39 (2014).
- [2] C. P. Brangwynne, C. R. Eckmann, D. S. Courson, A. Rybarska, C. Hoege, J. Gharakhani, F. Jlicher, and A. A. Hyman, *Science* **324**, 1729 (2009).
- [3] C. P. Brangwynne, T. J. Mitchison, and A. A. Hyman, *Proceedings of the National Academy of Sciences* **108**, 4334 (2011).
- [4] N. Gilks, N. Kedersha, M. Ayodele, L. Shen, G. Stoecklin, L. M. Dember, and P. Anderson, *Molecular Biology of the Cell* **15**, 5383 (2004).
- [5] A. Patel, H. O. Lee, L. Jawerth, S. Maharana, M. Jahnel, M. Y. Hein, S. Stoykov, J. Mahamid, S. Saha, T. M. Franzmann, A. Pozniakovski, I. Poser, N. Maghelli, L. A. Royer, M. Weigert, E. W. Myers, S. Grill, D. Drechsel, A. A. Hyman, and S. Alberti, *Cell* **162**, 1066 (2015).
- [6] S. Saha, C. A. Weber, M. Nusch, O. Adame-Arana, C. Hoege, M. Y. Hein, E. Osborne-Nishimura, J. Mahamid, M. Jahnel, L. Jawerth, A. Pozniakovski, C. R. Eckmann, F. Jlicher, and A. A. Hyman, *Cell* **166**, 1572 (2016).
- [7] Y. Lin, D. S. W. Protter, M. K. Rosen, and R. Parker, *Molecular Cell* **60**, 208 (2015).
- [8] S. F. Banani, A. M. Rice, W. B. Peeples, Y. Lin, S. Jain, R. Parker, and M. K. Rosen, *Cell* **166**, 651 (2016).
- [9] T. kami, S. Qamar, J. Q. Lin, G. S. K. Schierle, E. Rees, A. Miyashita, A. R. Costa, R. B. Dodd, F. T. S. Chan, C. H. Michel, D. Kronenberg-Versteeg, Y. Li, S.-P. Yang, Y. Wakutani, W. Meadows, R. R. Ferry, L. Dong, G. G. Tartaglia, G. Favrin, W.-L. Lin, D. W. Dickson, M. Zhen, D. Ron, G. Schmitt-Ulms, P. E. Fraser, N. A. Shneider, C. Holt, M. Vendruscolo, C. F. Kaminski, and P. St George-Hyslop, *Neuron* **88**, 678 (2015).
- [10] T. Nott, E. Petsalaki, P. Farber, D. Jervis, E. Fussner, A. Plochowitz, T. D. Craggs, D. Bazett-Jones, T. Pawson, J. Forman-Kay, and A. Baldwin, *Molecular Cell* **57**, 936 (2015).
- [11] S. T. Aoki, A. M. Kershner, C. A. Bingman, M. Wickens, and J. Kimble, *Proceedings of the National Academy of Sciences* **113**, 1279 (2016).
- [12] S. Elbaum-Garfinkle, Y. Kim, K. Szczepaniak, C. C.-H. Chen, C. R. Eckmann, S. Myong, and C. P. Brangwynne, *Proceedings of the National Academy of Sciences* **112**, 7189 (2015).
- [13] A. Molliex, J. Temirov, J. Lee, M. Coughlin, A. P. Kanagaraj, H. J. Kim, T. Mittag, and J. P. Taylor, *Cell* **163**, 123 (2015).
- [14] C. P. Brangwynne, P. Tompa, and R. V. Pappu, *Nature Physics* **11**, 899 (2015).
- [15] H. N. W. Lekkerkerker, V. W. A. De Villeneuve, J. W. J. De Folter, M. Schmidt, Y. Hennequin, D. Bonn, J. O. Indekeu, and D. Aarts, *The European Physical Journal B* **64**, 341 (2008).
- [16] H. N. W. Lekkerkerker, V. W. A. d. Villeneuve, J. W. J. d. Folter, M. Schmidt, Y. Hennequin, D. Bonn, J. O. Indekeu, and D. G. a. L. Aarts, *European Physical Journal B* **64**, 341 (2008).
- [17] E. Spruijt, J. Sprakel, M. Lemmers, M. A. C. Stuart, and J. van der Gucht, *Physical Review Letters* **105**, 208301 (2010).
- [18] E. Spruijt, J. Sprakel, M. A. C. Stuart, and J. v. d. Gucht, *Soft Matter* **6**, 172 (2010).

Supplementary Material

Salt-dependent rheology and surface tension of protein condensates using optical traps

Louise Jawerth^{*,1,2} Mahdiye Ijavi,¹ Martine Ruer,¹ Shambaditya Saha,¹ Marcus Jahnel,^{1,3} Anthony A Hyman,¹ Frank Jülicher,² and E. Fischer-Friedrich^{3,1,2}

¹Max-Planck-Institut für Zellbiologie und Genetik, Pfotenhauerstraße 108, 01307 Dresden, Germany

²Max-Planck-Institut für Physik komplexer Systeme, Nöthnitzerstraße 38, 01187 Dresden, Germany

³Biotechnology Center, Technische Universität Dresden, Tatzberg 47-49, 01307 Dresden, Germany

MATERIALS AND METHODS

Protein preparation. We use the protein purification protocol presented in Saha *et al.*¹. Untagged PGL-3 was further purified with HiLoad 16/60 Superdex 200 size-exclusion chromatography column (GE Healthcare) in size exclusion buffer. Untagged PGL-3 was stored in the same conditions as tagged PGL-3 (storage buffer: 25mM HEPES pH 7.5, 0.3M KCl, 1mM DTT). We added a small fraction of polystyrene beads (ThermoFisher, FluoSpheresTM F8887) of a diameter of $1\ \mu\text{m}$ to a buffer which lacked KCl. The PGL-3 droplet assembly was initiated through dilution of PGL3 in storage buffer using the bead solution to reach the desired, final salt concentration. This resulted in a buffer solution with many $\sim 10\ \mu\text{m}$ droplets with associated immersed beads (final buffer: 25mM HEPES, 1mM DTT, specified KCL, pH 7.5). Shortly after assembly, $1 - 2\ \mu\text{l}$ of the droplet solution was pipetted between two glass coverslips separated by a $100\ \mu\text{m}$ spacer. The bottom glass coverslip was PEG-passivated to minimize droplet adhesion. Elsewhere on the same sample chip, we also pipette $1 - 2\ \mu\text{l}$ of beads in a buffer which does not contain protein. We use beads in this region to thermally calibrate trap stiffnesses.

For the confocal image in Fig. 1b, main text and Movie 1, we follow the procedure above with the exception that we use protein before the GFP-tag cleavage step. The image is obtained using the built-in confocal of the optical trap and a 488 nm laser illumination.

Measurement setup. The sample chamber was loaded into the dual-trap optical trap (C-TrapTM, LUMICKS) and all measurements were made within two hours of droplet formation. Optical trap stiffness was determined by fitting a Lorentzian function to the power spectral density of the fluctuations of a trapped bead² using the built-in thermal calibration routine of the optical trap; for this calibration, beads without associated protein droplets were used. Trap stiffnesses were in the range of $140 - 170\ \text{pN}/\mu\text{m}$ for salt concentrations 75-150 mM. We reduced laser powers of the optical trap at salt concentration 180 mM to avoid laser induced artifacts that we attribute to heating. This resulted in trap stiffnesses of $60 - 80\ \text{pN}/\mu\text{m}$ at 180 mM salt concentration.

To measure the rheological properties of a droplet, we trapped a single bead in each of the two traps; both beads were immersed in a large droplet. We moved the trap centers apart until the droplet was slightly stretched. We applied an oscillatory strain at several predefined frequencies to protein droplets while measuring the corresponding force.

To illustrate droplet manipulation in the optical trap, a time-lapse of a GFP-tagged droplet being pulled apart with $2\ \mu\text{m}$ diameter beads is shown in Movie 1.

Trap calibration. During the experiments, we calibrated the optical trap with a naked bead inside aqueous buffer solution obtaining trap stiffness k and sensitivity $1/\beta$. We find that the conversion factor $k\beta$ between force and voltage is largely independent (within 10%) of bead size and has the same value if a bead is replaced by droplets of different size. This is consistent with previous reports showing that this conversion factor is independent of the specific conditions of the experiment, but is a feature of the instrument³.

The trap stiffness k is dependent on bead size and refractive index. To test whether the presence of the droplet influences the value of k during our measurements, we measure the system spring constant χ_{sys}^* using the conversion factor $k\beta$ (Fig. 1a, main text). For the case of the droplet spring constant χ^* being significantly larger in magnitude than the stiffnesses of the optical traps, the droplet provides a quasi-rigid linker between the two beads in the optical traps. Since the displacement of the trap center is imposed, we can, in this case, determine the actual value of the spring constant of the two traps in series $k_1k_2/(k_1+k_2)$ independently as the value of χ_{sys}^* . This situation is expected to be realized for the case of small k_1, k_2 and for large values of χ_{sys}^* which we find in the high frequency regime (Fig. 3a, main text). Indeed, we observed that the maximal value of χ_{sys}^* converges to $k_1k_2/(k_1+k_2)$ for spring constants $k_1, k_2 \lesssim 60\ \text{pN}/\mu\text{m}$, where k_1 and k_2 are the spring constants determined from the calibration with naked beads (see

Fig. 1). If the presence of the droplet material would have altered the trap stiffnesses, these values would not have agreed. In summary, this shows that both the conversion factor and the trap stiffness are largely unchanged by the presence of the droplet within the measurement error.

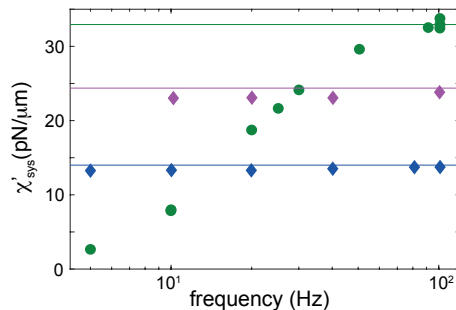


FIG. 1. At high frequencies, the system spring constant χ_{sys}^* (rhombi: 75 mM KCL, circles: 200 mM KCl) approaches the predicted limit value of the combined traps in series $k_1 k_2 / (k_1 + k_2)$ (solid lines, green: $k_1 = k_2 = 66$ pN/ μm , pink: $k_1 = k_2 = 49$ pN/ μm , blue: $k_1 = k_2 = 28$ pN/ μm) as the droplet spring constant becomes considerably larger than trap stiffnesses. Spring constants were determined from the calibration of naked beads.

Data analysis. During measurements, the position of the movable trap center x_1 and the forces exerted by the two traps F_1 and F_2 were recorded. It is important to note that $x_1 = C + x_{sys}$ (Fig. 1c, main text), where C is a constant. Therefore, the time-periodic change in the system's length x_{sys} equals the time-periodic change in x_1 during measurements. The inter-bead distance d_b between the two trapped beads was obtained through a LUMICKS C-trap built-in image analysis algorithm. From the time-average of the inter-bead distance $\langle d_b \rangle$, we determined the average protein droplet radius as $R = \langle d_b \rangle / 2 + r_{bead}$, where r_{bead} was the bead radius. The corresponding droplet radius R was confirmed by brightfield images of droplets.

We first determined the one-dimensional rheological response of the two traps in series with the droplet using $\sigma = (F_1 - F_2)/2$ as stress variable. The corresponding time-periodic stress signal and the time-periodic trap distance x_{sys} were fit by sinusoidal curves to determine the amplitudes A_σ and $A_{x_{sys}}$ and phase φ_σ and $\varphi_{x_{sys}}$ of either signal. The spring constant of the system χ_{sys}^* was then calculated as $A_\sigma / A_{x_{sys}} \exp(i(\varphi_\sigma - \varphi_{x_{sys}}))$ (Fig. 1a, main text). We then calculated the droplet spring constant χ^* from Eq. (5), main text. The hydrodynamic drag coefficient of the droplet was estimated as the Stokes drag $\xi = 6\pi R\eta_b$, where $\eta_b = 10^{-3}$ Pa s is the viscosity of the buffer. Using the droplet spring constant χ^* , we identified (by eye) a low frequency regime, where the storage modulus dominates and is constant. In this regime, our theoretical considerations indicate that surface tension dominates (Fig. 2a,b, main text). For our measurements, this regime was identified as $f \leq 0.2$ Hz (Fig. 3a, main text). We averaged the measured storage moduli in this frequency regime and determined surface tension by use of Eq. (16). There, we set $\theta_0 = r_{bead}/R$ where r_{bead} is the radius of the trapped polystyrene beads and R is the radius of the droplet. Furthermore, we identified a high-frequency regime where the real part of the droplet spring constant χ^* significantly exceeds the surface-tension-plateau (Fig. 3a, main text). For our measurements, this regime was identified as $f \geq 4$ Hz. In this high-frequency regime, we used the expansion Eqn. (18) to calculate G^* (see also Eq. 10, main text). In addition, we determined the loss modulus of the droplet for the frequency range $f < 4$ Hz by numerically solving Eq. (19) as in this regime $G' \ll G''$.

Passive bead-tracking microrheology. We performed passive bead-tracking microrheology to measure viscosity independently by an established method. We quantified the thermal motion of immersed microspheres (1 μm diameter) in large droplets of protein condensate at an exemplary salt concentration of 75 mM (Fig. 2a). To this end, we generated large protein droplets as described in the subsequent paragraph. By analyzing the thermal motion of immersed beads over time, we obtain a mean-square-displacement $\langle r^2(\tau) \rangle$ (Fig. 2b). We find that the time-dependence of $\langle r^2(\tau) \rangle$ is captured well by a linear fit with a slope of $4D \approx 0.0025$ $\mu\text{m}^2/\text{s}$, where D is the diffusion coefficient. From the Stokes-Einstein relation, we find $D = k_B T / (6\pi\eta r)$, where D is the diffusion constant and r is the radius of the bead. The corresponding viscosity estimate is $\eta \approx 0.7$ Pa s of the protein condensate at 75 mM salt concentration.

Experimental details: We loaded 25 μl of PGL-3 in a high salt (300 mM KCl) buffer into a custom-made chamber that incorporates a dialysis membrane; this chamber allows buffer exchange while simultaneously imaging the sample through a glass bottom. Before addition to the chamber, we also added a small fraction of 1 μm diameter red-

fluorescent beads (ThermoFisher, FluoSpheresTM F8887) to the protein solution. Both the beads and glass coverslip were coated with poly-ethylene glycol (PEG) to minimize adhesion between these surfaces and the protein. Droplet assembly was initiated by changing buffer conditions such that there is a final salt concentration of 75 mM KCl. We wait ~ 30 min to allow most coalescence events to cease. Subsequently, we acquire image stacks representing the three-dimensional volume surrounding a large ($\sim 30 \mu\text{m}$ radius) droplet with a voxel size of $0.136 \times 0.136 \times 0.4 \mu\text{m}$ at a rate of 4 seconds per stack for over 2 hours. To analyze the motion of the beads, we created a maximum projection in the Z-direction of the droplet mid-section for each image stack acquired; for an imaging volume with a small number of bright points, this results in an image that represents the projection of features onto the x - y plane, effectively removing the z -component of their motion. We repeat this procedure at every time point to create a movie of the bead motion in x - y . We use the TrackMate algorithm (through Fiji plugin) to locate particle positions over time from the aligned image stack using sub-pixel localization resulting in a list of x, y positions over waiting time. We only analyze bead tracks that are longer than 1000 frames (4000 s). Moreover, we identify all beads that are close to the surface of the droplet and do not consider these for bead diffusion analysis.

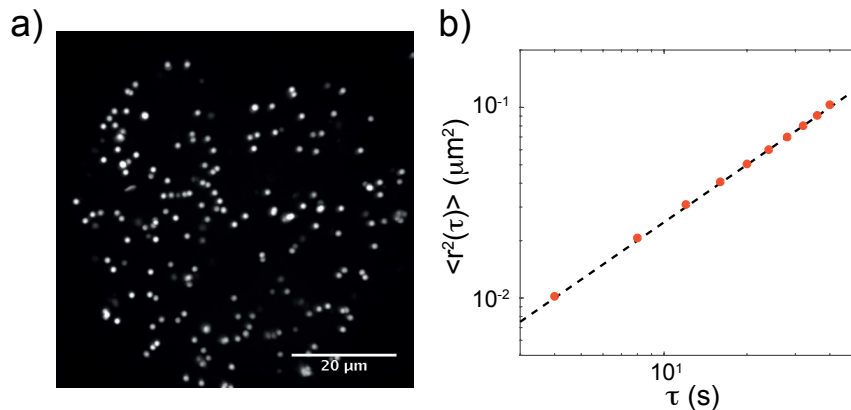


FIG. 2. Thermal motion of immersed microspheres (diameter: $1 \mu\text{m}$). a) Maximum intensity projection of a confocal z-stack of the mid-section of a protein droplet (not directly visible) with immersed fluorescent beads at salt concentration of 75 mM. b) Mean squared displacement of microspheres inside the protein droplet (red data points). The dashed black line shows a linear fit $4D\tau$ with a slope of $4D \approx 0.0025 \mu\text{m}^2/\text{s}$.

Analysis of droplet shape fluctuations. We also performed an analysis of droplet shape fluctuations to measure droplet surface tension independently by an established method. For this purpose, we quantified the Fourier modes of capillary waves of a protein droplet at a salt concentration of 180 mM. At high salt concentration, noticeable droplet shape fluctuations are present (see Movies 1 and 2). From a time-lapse brightfield movie of a droplet, we analysed droplet shape fluctuations normal to the surface boundary. The movie of a total time of 5.91 s was recorded with a 60x water immersion objective (NA 1.2) at a time interval of 0.01 s and a pixel size of 90 nm. We then performed image processing on this movie using Fiji⁴ (see Fig. 3): First, we inverted the image and then binarized it by using the ‘Auto local Threshold’ plugin (Method: Bernsen, radius: 10, parameter 1: 20, parameter 2: 0). To the obtained binary image, we applied the ‘Analyze Particles’ plugin detecting the outline of ‘particles’ with a size larger than 50 pixel². The obtained (inner) top and bottom outline of the droplet shape was then used to detect Fourier modes of boundary fluctuations in direction normal to the surface.

Shape fluctuations of an unperturbed spherical droplet of radius R may be described as an expansion in spherical harmonics⁵

$$r(\theta, \varphi, t) = R \left(1 + \sum_{l=2}^{l=l_{max}} \left\{ a_{l,0}(t) Y_{l,0}(\theta, \varphi) + \sum_{m=1}^l \left[\alpha_{l,m}(t) ((-1)^m Y_{l,m} + Y_{l,-m}) + \frac{\beta_{l,m}(t)}{i} ((-1)^m Y_{l,m} - Y_{l,-m}) \right] \right\} \right), \quad (1)$$

where $Y_{l,m}(\theta, \varphi)$ is the spherical harmonics function of degree l and order m . Surface fluctuations give rise to fluctuations in the surface energy^{5,6}

$$\delta\Phi = \frac{1}{2} \gamma R^2 [l(l+1) - 2] \left(a_{l,0}^2 + \sum_{m=1}^l (\alpha_{l,m}^2 + \beta_{l,m}^2) \right).$$

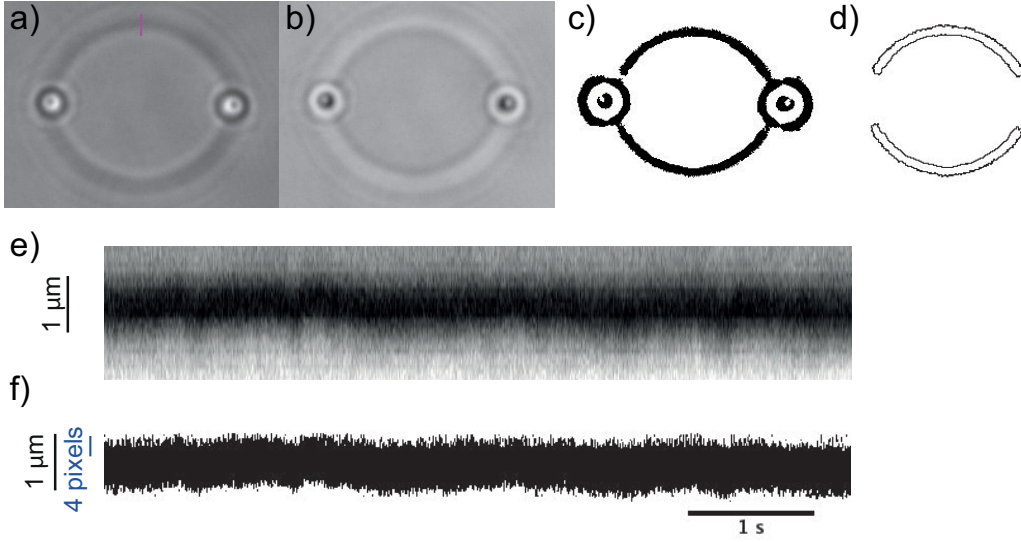


FIG. 3. Illustration of image processing steps of droplet micrographs (a-d) and droplet boundary fluctuations (e-f). a) Original image. b) Inverted image. c) Binarized image after local thresholding. d) Outlines obtained from particle analysis. e) Illustration of boundary fluctuations over time from a line scan along the pink line depicted in panel a. f) Thresholded version of boundary fluctuations from d.

According to the equipartition theorem, we have⁵

$$\langle \alpha_{lm}^2 \rangle = \langle \beta_{lm}^2 \rangle = \frac{k_B T}{(\gamma R^2 [l(l+1) - 2])}.$$

For the situation of a droplet held laterally by trapped, adherent beads, we assume that modes which have a non-vanishing amplitude at the position of the beads ($\theta = 0, \pi$) vanish. This assumption is corroborated by our analysis of surface fluctuations from the recorded time lapse movie. Therefore, we set $a_{l,0} = 0$. According to Eq. (1), we find for the radius fluctuations along the cross-section of $\varphi = 0$

$$\delta r(\theta, 0, t) = R \sum_{l=2}^{l=l_{max}} \sum_{m=1}^l (-1)^m 2\alpha_{l,m} Y_{l,m}(\theta, 0)$$

Let the Fourier decomposition of $\delta r(\theta, 0, t)$ be

$$\delta r(\theta, 0, t) = \sum_{n=1}^{\infty} (a_n(t) \cos(2n\theta) + b_n(t) \sin(2n\theta))$$

and let $c_n = \sqrt{a_n^2 + b_n^2}$. Then, the time-average $\langle c_n^2 \rangle$ is

$$\begin{aligned} \langle c_n^2 \rangle &= R^2 \sum_{l=2}^{l=l_{max}} \sum_{m=1}^l 4 \langle \alpha_{l,m}^2 \rangle \{F_{n,l,m,1}^2 + F_{n,l,m,2}^2\} \\ &= \sum_{l=2}^{l=l_{max}} \frac{4k_B T}{(\gamma [l(l+1) - 2])} \sum_{m=1}^l \{F_{n,l,m,1}^2 + F_{n,l,m,2}^2\}, \end{aligned}$$

with $F_{n,m,l,1} = \frac{2}{\pi} \int_0^\pi Y_{l,m}(\theta, 0) \cos(2n\theta) d\theta$ and $F_{n,m,l,2} = \frac{2}{\pi} \int_0^\pi Y_{l,m}(\theta, 0) \sin(2n\theta) d\theta$ the Fourier coefficients of the function $Y_{l,m}(\theta, 0)$. For our analysis, we approximated $\langle c_n^2 \rangle$ as

$$\langle c_n^2 \rangle \approx \sum_{l=2}^{l=15} \frac{4k_B T}{(\gamma [l(l+1) - 2])} \sum_{m=1}^l \{F_{n,l,m,1}^2 + F_{n,l,m,2}^2\}$$

for Fourier coefficients up to $n = 5$. The obtained values of $\langle c_n^2 \rangle$ and the associated estimates of γ as

$$\gamma \approx \frac{1}{\langle c_n^2 \rangle} \sum_{l=2}^{l=15} \frac{4k_B T}{([l(l+1) - 2])} \sum_{m=1}^l \{F_{n,l,m,1}^2 + F_{n,l,m,2}^2\}$$

are depicted in Fig. 4a and b, respectively. Our estimates of $\langle c_n^2 \rangle$ are well above the noise floor, which we estimate to be 300 nm^2 from the apparent boundary fluctuations of the imaged bead in our time lapse movie. The obtained surface tension estimates of $\approx 1.4 \mu\text{N/m}$ are indeed largely constant and agree to a good extent with the corresponding tweezer measurements at salt concentration 180 mM which gave a surface tension estimate of $\approx 1 \mu\text{N/m}$. From the decay of the autocorrelation function of the Fourier coefficients a_n and b_n , we estimate a characteristic decay time $\tau_{relax} \approx 0.13 \text{ s}$ (Fig. 4c). We know that $\tau_{relax} \propto \gamma/(\eta R)$, where R is the droplet radius and η its viscosity. This allows to make an order of magnitude estimate of η as $\tau_{relax} \gamma/R$. Measuring $R \approx 6.9 \mu\text{m}$, we obtain $\eta \approx 0.026 \text{ Pa s}$, which is indeed on the same order of magnitude as our tweezer measurement result of 0.07 Pa s at salt concentration of 180 mM (see Fig. 3g, main text).

We believe that our estimate of surface tension through capillary wave analysis is a coarse estimate of surface tension as our analysis predicts mean squared fluctuations of the shape that are well below the limit of optical resolution ($\langle c_1^2 \rangle \approx (40 \text{ nm})^2$). In this case, Fourier mode analysis of capillary waves most likely underestimates values of $\langle c_n^2 \rangle$ and thus overestimates γ .

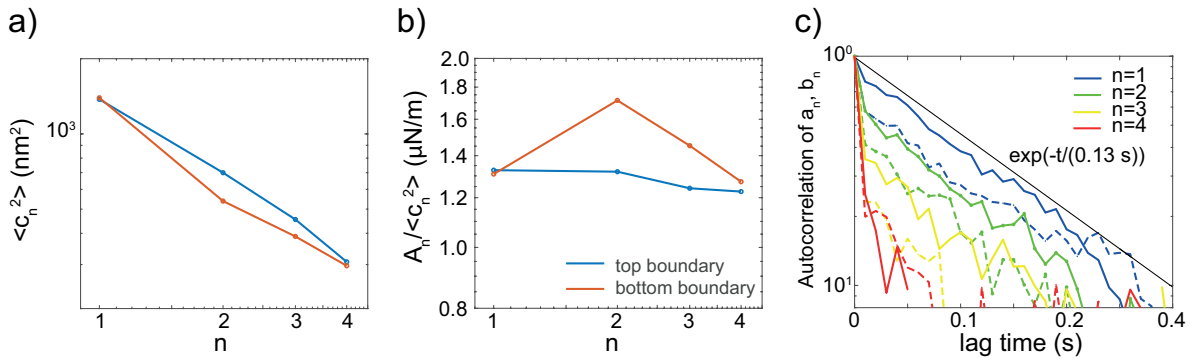


FIG. 4. Shape fluctuations of a protein droplet at salt concentration 180 mM. a) Time-averaged squared Fourier coefficients c_n of shape fluctuations normal to the droplet boundary. b) Surface tension estimate for different Fourier coefficients according to the formula $A_n / \langle c_n^2 \rangle$ where $A_n = \sum_{l=2}^{l=15} 4k_B T / ([l(l+1) - 2]) \sum_{m=1}^l \{F_{n,l,m,1}^2 + F_{n,l,m,2}^2\}$. c) Autocorrelation of the Fourier coefficients a_n (solid line) and b_n (dashed line). We find a characteristic slowest decay time of $\approx 0.13 \text{ s}$.

CONTINUUM MECHANICS THEORY OF OPTICAL TRAP MICRORHEOLOGY

In this section, we estimate the deformation response of a micron-sized spherical viscoelastic droplet immersed in a surrounding liquid of significantly lower viscosity. The droplet is subject to an oscillatory pressure applied with angular frequency ω in two dome-shaped regions at its poles (Fig. 2a, main text). We will determine the complex frequency-dependent spring constant of uniaxial droplet deformation $\chi^*(\omega)$ in dependence of surface tension γ and complex shear modulus $G^*(\omega)$ of the droplet material. For this purpose, we will perform a perturbation equation to first order in stress, strain and deformation. We choose the coordinate system such that the problem is rotationally symmetric with respect to the z -axis (Fig. 2, main text) and there is no dependence on the displacement on the azimuthal angle φ . The radial and axial displacement of the droplet u_r and u_θ , the associated internal velocities v_r and v_θ and the internal pressure change δp are time-dependent. As we are interested in the calculation of the displacement and the velocities to first order, the governing equations are linear. Thus, time dependence can be factorised and we can write

$$u_{r,\theta}(r, \theta, t) = \tilde{u}(r, \theta) \exp(i\omega t) + c.c. \quad (2)$$

$$v_{r,\theta}(r, \theta, t) = i\omega \tilde{u}_{r,\theta}(r, \theta) \exp(i\omega t) + c.c. \quad (3)$$

$$\delta p(r, \theta, t) = \delta \tilde{p}(r, \theta) \exp(i\omega t) + c.c. \quad (4)$$

Here, the tilde denotes the complex amplitude of the Fourier mode at angular frequency ω and $c.c.$ refers to the complex conjugate. In the following, we will leave out the tilde above u , v and p keeping in mind that the time

dependence of these functions is captured by a simple time-periodic modulation. Furthermore, we will omit the expression “+c.c.” for convenience.

The Reynolds number of the hydrodynamic problem under consideration is $Re = \rho v R / \eta$ where R is the droplet radius. The fluid velocity may be estimated as $v \approx \omega R$. Assuming a droplet of $R \leq 10 \mu\text{m}$, a density similar to water $\rho \approx 1000 \text{ kg/m}^3$, frequencies $f \leq 100 \text{ Hz}$ and $\eta > 10^{-3} \text{ Pa s}$, we obtain as an upper bound estimate for the Reynolds number $Re \lesssim 10^{-2}$ which is $\ll 1$. Therefore, we will consider the dynamics of the fluid constituting the droplet as over-damped.

Force balance and incompressibility requires (in Cartesian coordinates) $\partial_i \sigma_{ij} = 0$ and $\partial_i v_i = 0$. For the viscoelastic stresses inside the incompressible droplet, we make the ansatz (in Cartesian coordinates)

$$\sigma_{ij} = -p \delta_{ij} + G^*(\omega) [\partial_i u_j + \partial_j u_i] \quad , \quad (5)$$

where $G^*(\omega)$ is the frequency-dependent complex elastic shear modulus of the droplet material. Note, that if the droplet is a Newtonian liquid with $G^*(\omega) = i\omega\eta$, the force balance equation equals the Stokes equation in Fourier space as $\underline{v} = i\omega\underline{u}$. In spherical coordinates, we obtain⁷

$$\frac{\partial p}{\partial r} = G^*(\omega) \left[\frac{1}{r^2} \frac{\partial}{\partial r} \left(r^2 \frac{\partial u_r}{\partial r} \right) + \frac{1}{r^2 \sin(\theta)} \frac{\partial}{\partial \theta} \left(\sin(\theta) \frac{\partial u_r}{\partial \theta} \right) - 2 \frac{u_r + \frac{\partial u_\theta}{\partial \theta} + u_\theta \cot(\theta)}{r^2} \right] \quad (6)$$

$$\frac{1}{r} \frac{\partial p}{\partial \theta} = G^*(\omega) \left[\frac{1}{r^2} \frac{\partial}{\partial r} \left(r^2 \frac{\partial u_\theta}{\partial r} \right) + \frac{1}{r^2 \sin(\theta)} \frac{\partial}{\partial \theta} \left(\sin(\theta) \frac{\partial u_\theta}{\partial \theta} \right) + \frac{2}{r^2} \frac{\partial u_r}{\partial \theta} - \frac{u_\theta}{r^2 \sin(\theta)^2} \right]. \quad (7)$$

As the viscosity of the droplet environment is assumed to be significantly lower than the droplets viscosity and velocities have to match at the phase boundary, viscous stresses outside the droplet are negligible and we set them to zero. Force balance at the droplet boundary imposes

$$-p_{ext} - \sigma_{rr}(R, \theta) = 2\gamma H, \quad (8)$$

$$\sigma_{r,\theta}(R, \theta) = 0 \quad (9)$$

where p_{ext} is the local normal force per area applied on the droplet externally through the oscillatory forcing at the poles and an external hydrostatic pressure. Furthermore, γ is the droplet's surface tension that gives rise to a pressure jump across the droplet boundary. The mean curvature of the droplet is denoted by H . If the droplet is unperturbed, it acquires a spherical shape with mean curvature $H = 1/R$. In this case, Eq. (8) states Laplace's law in the form $-p_{ext} + p = 2\gamma/R$, where p_{ext} is a constant external hydrostatic pressure. If the droplet is slightly deformed from the spherical shape in terms of a displacement $(r, \theta) \rightarrow (r + u_r, \theta + u_\theta)$ through oscillatory forcing at the poles, one may express the change in the mean curvature of the droplet surface to first order in the displacement by $-(2u_r + \partial_\theta u_r \cot \theta + \partial_\theta^2 u_r)/(2R^2)$ ⁸.

Substituting $\sigma_{rr} = -p + 2G^*(\omega)\partial_r u_r$ and $\sigma_{r,\theta}(r, \theta) = G^*(\omega) \left(\frac{1}{r} \frac{\partial u_r}{\partial \theta} + \frac{\partial u_\theta}{\partial r} - \frac{u_\theta}{r} \right)$ ⁹ into Eqn. (8),(9), we obtain

$$-\delta p_{ext} = \left(-\gamma(2u_r + \partial_\theta u_r \cot \theta + \partial_\theta^2 u_r)/R^2 - \delta p + 2G^*(\omega)\partial_r u_r \right) \Big|_{r=R} \quad (10)$$

$$0 = G^*(\omega) \left(\frac{1}{r} \frac{\partial u_r}{\partial \theta} + \frac{\partial u_\theta}{\partial r} - \frac{u_\theta}{r} \right) \Big|_{r=R}, \quad (11)$$

where δp and δp_{ext} are the change of the internal and external pressure change, respectively. To solve Eqn. (8, 9), we use a stream function approach

$$i\omega u_r = -\frac{1}{r^2 \sin(\theta)} \frac{\partial \psi}{\partial \theta}, \quad i\omega u_\theta = \frac{1}{r \sin(\theta)} \frac{\partial \psi}{\partial r}.$$

A solution to Eqn. (8, 9) with the correct symmetries of the problem is given by the ansatz¹⁰

$$\psi(r, \theta) = \sum_{n=3, n \text{ odd}}^{\infty} \frac{P_{n-2}(\cos \theta) - P_n(\cos \theta)}{2n-1} \left(A_n \frac{r^n}{R^{n-2}} + C_n \frac{r^{n+2}}{R^n} \right)$$

giving rise to the solutions

$$\begin{aligned}
i\omega u_r = v_r &= - \sum_{n=3, n \text{ odd}}^{\infty} P_{n-1}(\cos \theta) \left(A_n \frac{r^{n-2}}{R^{n-2}} + C_n \frac{r^n}{R^n} \right) \\
i\omega u_\theta = v_\theta &= \sum_{n=3, n \text{ odd}}^{\infty} \frac{P_{n-2}(\cos \theta) - P_n(\cos \theta)}{(2n-1) \sin \theta} \left(n A_n \frac{r^{n-2}}{R^{n-2}} + (n+2) C_n \frac{r^n}{R^n} \right) \\
\delta p &= - \frac{G^*(\omega)}{i\omega} \sum_{n=3, n \text{ odd}}^{\infty} P_{n-1}(\cos \theta) \frac{2(2n+1)}{(n-1)} C_n \frac{r^{n-1}}{R^n}
\end{aligned} \tag{12}$$

where P_n is the Legendre polynomial of n -th degree. This solution of the flow field inside the sphere needs to be matched with the boundary conditions given by Eqn. (10) and (11) for the applied change of external pressure $\delta p_{ext}(\theta)$ by an adequate match of the coefficients A_n and C_n . To achieve this, an expansion of the external pressure change in terms of Legendre polynomials is calculated

$$\delta p_{ext} = \sum_{n=3, n \text{ odd}}^{\infty} X^{n-1} P_{n-1}(\cos \theta)$$

where

$$X^n = \frac{2n+1}{2} \int_0^\pi \delta p_{ext}(\theta) P_{n-1}(\cos \theta) \sin(\theta) d\theta \quad .$$

For the problem under consideration, the external pressure is given by an even pressure applied at two symmetric caps at the poles of the sphere. Thus,

$$\delta p_{ext}(\theta) = P_0 \{ \Theta(\theta - \pi + \theta_0) + \Theta(\theta_0 - \theta) \}.$$

We have solved the system of equations for A_n and C_n up to index $n = 11$, truncating the expansion after this. As solutions, we obtain

$$\begin{aligned}
A_3 &= \frac{(20P_0R^2\omega \cos(\theta_0) \sin(\theta_0)^2)}{i(-20\gamma - 19RG^*)} \\
C_3 &= \frac{(15P_0R^2\omega \cos(\theta_0) \sin(\theta_0)^2)}{i(40\gamma + 38RG^*)} \\
A_5 &= \frac{(3P_0R^2\omega \cos(\theta_0)(1 + 7 \cos(2\theta_0)) \sin(\theta_0)^2)}{i(-36\gamma - 17RG^*)}, \\
C_5 &= \frac{-((15P_0R^2\omega \cos(\theta_0)(1 + 7 \cos(2\theta_0)) \sin(\theta_0)^2)}{(8i(-36\gamma - 17RG^*))} \\
A_7 &= \frac{(39P_0R^2\omega \cos(\theta_0)(19 + 12 \cos(2\theta_0) + 33 \cos(4\theta_0)) \sin(\theta_0)^2)}{(40i(-104\gamma - 33RG^*))} \\
C_7 &= \frac{-((91P_0R^2\omega \cos(\theta_0)(19 + 12 \cos(2\theta_0) + 33 \cos(4\theta_0)) \sin(\theta_0)^2)}{(128i(-104\gamma - 33RG^*))} \\
A_9 &= \frac{(85P_0R^2\omega \cos(\theta_0)(178 + 869 \cos(2\theta_0) + 286 \cos(4\theta_0) + 715 \cos(6\theta_0)) \sin(\theta_0)^2)}{(448i(-680\gamma - 163RG^*))} \\
C_9 &= \frac{-((153P_0R^2\omega \cos(\theta_0)(178 + 869 \cos(2\theta_0) + 286 \cos(4\theta_0) + 715 \cos(6\theta_0)) \sin(\theta_0)^2)}{(1024i(-680\gamma - 163RG^*))} \\
A_{11} &= \frac{(175P_0R^2\omega \cos(\theta_0)(2773 + 2392 \cos(2\theta_0) + 5252 \cos(4\theta_0) + 1768 \cos(6\theta_0) + 4199 \cos(8\theta_0)) \sin(\theta_0)^2)}{(36864i(-140\gamma - 27RG^*))} \\
C_{11} &= \frac{-((385P_0R^2\omega \cos(\theta_0)(2773 + 2392 \cos(2\theta_0) + 5252 \cos(4\theta_0) + 1768 \cos(6\theta_0) + 4199 \cos(8\theta_0)) \sin(\theta_0)^2)}{(98304i(-140\gamma - 27RG^*))}
\end{aligned} \tag{13}$$

To calculate the effective one-dimensional rheology of the droplet during oscillatory deformations along the z -axis, we determine the amplitude of the force applied to the left and right pole $P_0 2\pi R^2 (1 - \cos(\theta_0))$ and the (complex)

amplitude of the radial displacement $u_r(R, \theta = 0)$. The one-dimensional complex elastic modulus of uniaxial droplet deformation is then

$$\chi^*(\omega) = P_0 2\pi R^2 (1 - \cos(\theta_0)) / (2u_r(R, 0)) \quad , \quad (14)$$

where we have used that $x_d = 2(R + u_r(R, 0))$ (Fig. 1c, main text). We obtain an expression for $\chi^*(\omega)$ in terms of the complex elastic modulus $G^*(\omega)$ of the droplet material and its surface tension γ using Eqn. (12), (13) and (14). While the full expression for $\chi^*(\omega)$ in dependence of $G^*(\omega)$ and γ is too voluminous to be printed here, we will give in the following explicit expressions for several limit cases.

1) Small complex elastic modulus

If surface tension γ is dominant in the effective one-dimensional storage modulus, one obtains the relation

$$\chi^*(\omega) \approx \frac{\gamma \csc(\theta_0)^2 (-9.98 + 4.98 \sec(\theta_0))}{2.32 + \cos(2\theta_0) + 0.42 \cos(4\theta_0) + 0.17 \cos(6\theta_0) + 0.08 \cos(8\theta_0)} \quad (15)$$

which simplifies for small θ_0 to

$$\chi^*(\omega) \approx \gamma(1.25 + 4.36\theta_0^2), \quad (16)$$

including contributions of θ_0 up to second order.

2) Small surface tension

If the influence of droplet surface tension γ is entirely negligible, our calculation yields

$$\chi^*(\omega) = \frac{25.36 \sec(\theta_0/2)^2 \sec(\theta_0) R G^*(\omega)}{16.23 + 13.68 \cos(2\theta_0) + 8.01 \cos(4\theta_0) + 3.73 \cos(6\theta_0) + 2.09 \cos(8\theta_0)}. \quad (17)$$

For small values of θ_0 and γ , we may perform a Taylor expansion of $\chi^*(\omega)/(R|G^*|)$ including contributions to first and second order, respectively, in $\gamma/(R|G^*|)$ and θ . This expansion yields the approximate relation

$$\chi^*(\omega) \approx (0.58 + 3.42\theta_0^2) R G^*(\omega) + (1.75 + 6.31\theta_0^2) \gamma \quad (18)$$

3) Dominantly fluid-like droplet rheology

For the case $G' \ll G''$ and small θ_0 , we obtain the relation

$$\begin{aligned} \chi'' \approx & \left[R\gamma^{16} (8.18 \cdot 10^2 + 4.16 \cdot 10^3 \theta_0^2) G'' + R^3 \gamma^{14} (1.09 \cdot 10^3 + 5.81 \cdot 10^3 \theta_0^2) G''^3 + R^5 \gamma^{12} (5.59 \cdot 10^2 + 3.09 \cdot 10^3 \theta_0^2) G''^5 + \right. \\ & R^7 \gamma^{10} (1.46 \cdot 10^2 + 8.22 \cdot 10^2 \theta_0^2) G''^7 + R^9 \gamma^8 (21.3 + 1.22 \cdot 10^2 \theta_0^2) G''^9 + R^{11} \gamma^6 (1.8 + 10.5 \theta_0^2) G''^{11} + \\ & \left. R^{13} \gamma^4 (8.78 \cdot 10^{-2} + 5.13 \cdot 10^{-1} \theta_0^2) G''^{13} + R^{15} \gamma^2 (2.26 \cdot 10^{-3} + 1.33 \cdot 10^{-2} \theta_0^2) G''^{15} + R^{17} (2.39 \cdot 10^{-5} + 1.41 \cdot 10^{-4} \theta_0^2) G''^{17} \right] \\ & / \left[31.83 \gamma^8 + 22.54 R^2 \gamma^6 G''^2 + 4.35 R^4 \gamma^4 G''^4 + 0.3 R^6 \gamma^2 G''^6 + 6.41 \cdot 10^{-3} R^8 G''^8 \right]^2 \quad , \quad (19) \end{aligned}$$

taking into account contributions in θ_0 up to second order.

In all above equations, numerical coefficients were rounded to two decimal places. In the Materials and Methods section of this document, we explain how Eqn. (16), (18) and (19) are used to analyse our data.

BIBLIOGRAPHY

- ¹S. Saha, C. A. Weber, M. Nousch, O. Adame-Arana, C. Hoege, M. Y. Hein, E. Osborne-Nishimura, J. Mahamid, M. Jahnel, L. Jawerth, et al., *Cell* **166**, 1572 (2016).
- ²P. H. Jones, O. M. Marag, and G. Volpe, *Optical Tweezers: Principles and Applications* (Cambridge University Press, 2015).
- ³A. Farr, F. Mars, and M. Montes-Usategui, *Optics Express* **20**, 12270 (2012).
- ⁴J. Schindelin, I. Arganda-Carreras, E. Frise, V. Kaynig, M. Longair, T. Pietzsch, S. Preibisch, C. Rueden, S. Saalfeld, and B. Schmid, *Nature methods* **9**, 676 (2012).
- ⁵S. Ljunggren and J. Christer Eriksson, *Journal of the Chemical Society, Faraday Transactions 2: Molecular and Chemical Physics* **80**, 489 (1984).
- ⁶T. Betz and C. Sykes, *Soft Matter* **8**, 5317 (2012).
- ⁷D. J. Acheson, *Elementary Fluid Dynamics* (Clarendon Press, 1990).
- ⁸A. Mietke, O. Otto, S. Girardo, P. Rosendahl, A. Taubenberger, S. Golfier, E. Ulbricht, S. Aland, J. Guck, and E. Fischer-Friedrich, *Biophys. J.* **109**, 2023 (2015).
- ⁹L. D. Landau and E. M. Lifshitz, *Fluid Mechanics* (Pergamon Press, 1987), 2nd ed.
- ¹⁰L. Haberman and R. Sayre, D. Taylor (Ed.), *Model Basin Rep.* (1958).
- ¹¹E. Spruijt, J. Sprakel, M. Lemmers, M. A. C. Stuart, and J. van der Gucht, *Physical Review Letters* **105**, 208301 (2010).

SUPPLEMENTARY FIGURES

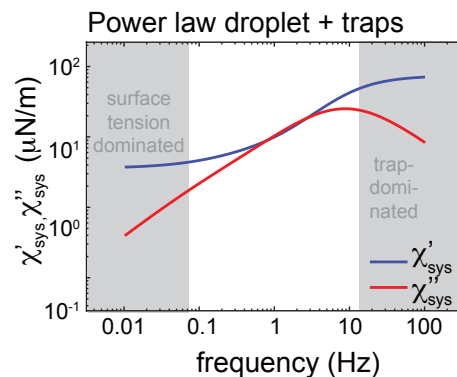


FIG. 5. Effective spring constant of the combined system of two identical traps in series with a power law droplet (spring constant $k = 150 \text{ pN}/\mu\text{m}$). For low frequencies, the force response of the power law droplet is dominated by surface tension (grey zone, l.h.s.). For high frequencies, the two traps dominate the force response of the model system and the effective spring constant approaches $k/2$ (grey zone, r.h.s.). Outside of this trap-dominated regime, the loss modulus is governed by the power law of the droplet material. Parameters are $\theta_0 = 0.1$, $R = 5 \mu\text{m}$, $\gamma = 3 \mu\text{N}/\text{m}$, $\eta = 0.5 \text{ Pas}$, $A = 0.2 \text{ Pa}$, $\beta = 0.8$.

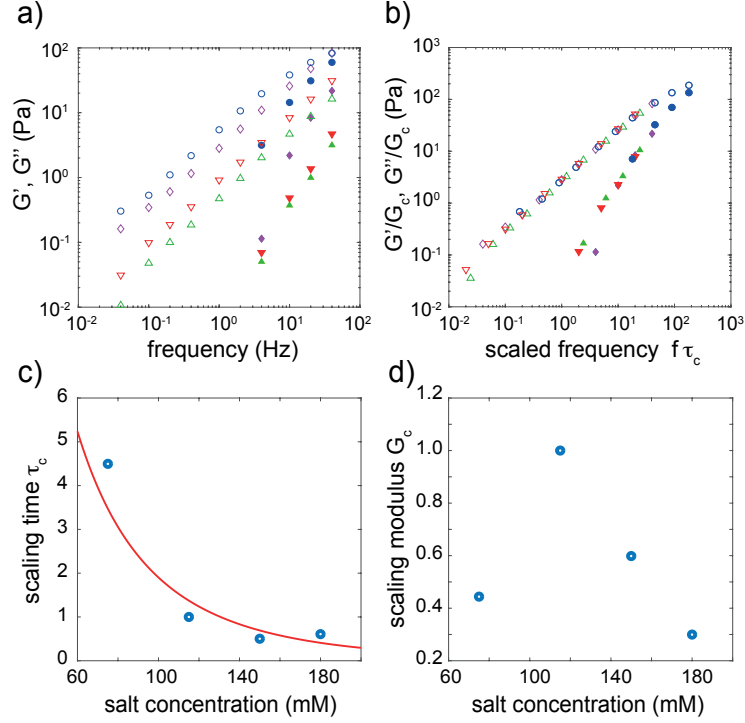


FIG. 6. (a-b) Complex elastic moduli of protein condensates in dependence of salt concentration can be collapsed on top of each other through rescaling of y-axis and x-axis by a factor G_c and τ_c , respectively. Panel a shows the uncollapsed data, while panel b shows collapsed data after rescaling (blue: 75 mM, purple: 115 mM, red: 150 mM, green: 180 mM, same data as main text). The collapse of rheological data at different salt concentrations through rescaling is analogous to previously reported findings for polyelectrolyte complexes¹¹. (c-d) Scaling parameters τ_c (c) and G_c (d) at different salt concentrations. In c, we have fitted a stretched exponential function $A \exp(-B(c/1000)^{1/2})$ (solid red line). This functional dependence on salt concentration was previously reported for time scales τ_c for polyelectrolyte complexes¹¹. We find fit constants of $A = 170.4s$ and $B = 14.22 M^{-1/2}$.

Supplemental Movie 1, caption: Confocal time-lapse movie of fluorescent protein droplet (blue, salt concentration 75 mM) and adherent beads (yellow). Beads are held by the optical traps. Movement of the mobile trap leads to bead displacement and droplet deformation. The frame interval is 0.5 s. The pixel size is 200 nm. Beads are $2 \mu\text{m}$ in size (for illustrative purposes) and the traps are moving apart at a rate of $0.002 \mu\text{m/s}$.

Supplemental Movie 2, caption: Brightfield time-lapse movie of a protein droplet (salt concentration 180 mM) held in place through two adherent beads which are trapped by the two optical traps. The droplet undergoes visible thermal shape fluctuations over time. The frame interval is 0.01 s. The pixel size is 90 nm.